## FUEL CELLS

# Oxygen- and proton-transporting open framework ionomer for medium-temperature fuel cells

Jianwei Yang[1], Hengyu Xu[2], Jie Li[1], Ke Gong[1], Feiyu Yue[1], Xianghao Han[1], Ke Wu[1], Pengpeng Shao[1], Qingling Fu[1], Yuhao Zhu[1], Wenli Xu[1], Xin Huang[1], Jing Xie[1], Fengchao Wang[2], Wenxiu Yang[1], Teng Zhang[1], Zengshi Xu[3], Xiao Feng[1]*, Bo Wang[1]*

Medium-temperature proton exchange membrane fuel cells (MT PEMFCs) operating at 100° to 120°C have improved kinetics, simplified thermal and water management, and broadened fuel tolerance compared with low-temperature PEMFCs. However, high temperatures lead to Nafion ionomer dehydration and exacerbate gas transportation limitations. Inspired by osmolytes found in hyperthermophiles, we developed α-aminoketone–linked covalent organic framework (COF) ionomers, interwoven with Nafion, to act as "breathable" proton conductors. This approach leverages synergistic hydrogen bonding to retain water, enhancing hydration and proton transport while reducing oxygen transport resistance. For commercial Pt/C, the MT PEMFCs achieved peak and rated power densities of 18.1 and 9.5 Watts per milligram of Pt at the cathode at 105°C fueled with $H_2$ and air, marking increases of 101 and 187%, respectively, compared with cells lacking the COF.

P roton exchange membrane fuel cells (PEMFCs) provide clean energy (1–6) but have limitations, particularly operating temperature. Elevating the working temperature of PEMFCs could improve performance in several ways: (i) It would enhance the activity of the catalyst and electrochemical kinetics (7); (ii) cooling could be simplified given a larger temperature differential between the coolant out and the ambient temperature (fig. S1); (iii) flooding at the cathode would be reduced (8), and (iv) the cell would be more tolerant of carbon monoxide, which would broaden the range of hydrogen sources (9). However, exceeding the 100°C threshold is challenging because of the phase transition of water, creating substantial proton conduction barriers in the membrane electrode assembly (MEA) (Fig. 1A) (10–12). High-temperature PEMFCs (≥120°C) that use phosphoric acids or imidazoles as the proton carriers (13–16) face difficulties such as proton carrier leakage and low power density. Medium-temperature PEMFCs (MT PEMFCs) that use water as the proton carrier could achieve high performance across low and medium operating temperature. The Japanese New Energy and Industrial Technology Development Organization (NEDO) has targeted increasing fuel cell operating temperatures to 105°C by 2030 and to 120°C by 2040 (17).

Strategies to bridge the proton conductivity gap at intermediate temperatures of 80° to 120°C include surface hydrophobic coating (18) and the development of short-side-chain perfluorosulfonic acid (PFSA)–based (19), sulfonated polyphenylenes–based (20), or sulfo-phenylated polyphenylene–based (21) proton conduction membranes or ionomers in the catalyst layer (CL). Despite these efforts, overcoming the pronounced decline in proton conductivity from dehydration and enhancing MT PEMFC performance remains challenging. Moreover, the rise in temperature further elevates the partial pressure of water and diminishes the partial pressure of oxygen (22, 23). This relative change intensifies local oxygen transport resistance, exacerbating the burden on traditional proton conductors in the CL (Fig. 1A). Recently, we identified covalent organic frameworks (COF) (24–28) as promising ionomers for enhancing oxygen transport efficiency in the CL of low-temperature PEMFCs (LT PEMFCs) (29). However, MT PEMFCs encounter severe challenges caused by the water phase transition and ionomers dehydration, which complicate the oxygen-water-catalyst three-phase microenvironment, obstruct the proton transport pathway, and heighten oxygen transport resistance.

Hyperthermophiles thrive under extreme heat, from 80° to 125°C (30, 31), performing respiration and producing energy similar to that of the operational requirement of MT PEMFCs. Their survival hinges on efficient gas exchange through lipid layers and the hydration maintained by osmolytes such as proline, isoleucine, and betaine, which feature α-aminoketone linkages (Fig. 1B) (32). Inspired by these organisms, we have engineered α-aminoketone–linked COFs (Am-COF) and interwove them with Nafion (Am-COF/Nafion) to create "breathable" proton conductors for MT PEMFCs.

In comparison to the sulfonic acid group in Nafion or COF, density functional theory (DFT) calculations revealed that neighboring carbonyl (C=O) groups in adjacent layers of COFs can simultaneously engage in intermolecular hydrogen bonding with water, substantially enhancing the water retaining capacity (Fig. 1C). Notably, unlike Nafion-based CL, the proton conductivity within the Am-COF–contained CL does not drop abruptly but rather increases for operating temperatures >100°C, ensuring uninterrupted proton conduction (Fig. 1D). Furthermore, the enhanced water retention and the porous apertures of the open framework ionomer reduced oxygen transport resistance in the CL. At 105°C, the MEA featuring Am-COF achieved peak and rated power densities at 0.67 V that were more than twice those of MEAs without the COF.

### Synthesis and characterization of breathable open framework ionomer

Efforts to synthesize crystalline Am-COFs through direct copolymerization of aromatic amines and α-aryl ketones were unsuccessful (tables S1 to S3). Thus, we converted imine linkages in COFs into α-aminoketone linkages through a linker exchange method, during which the COF crystallization process and irreversible bond formation were separated (33, 34). Initially, we used TAPB-BPDA-COF (35) (fig. S2, scheme S1), constructed from 5′-(4-aminophenyl)-[1,1′:3′,1″-terphenyl]-4,4″-diamine (TAPB) and [1,1′-biphenyl]-4,4′-dicarbaldehyde (BPDA), to react with 1,1′-([1,1′-biphenyl]-4,4′-diyl)bis(2-bromoethan-1-one) (BDBP). We systematically optimized the reaction conditions (figs. S3 to S5) to balance the hydrolysis of imine bonds and the formation of α-aminoketone linkages, resulting in crystalline Am-COF-1.

To validate the generality of this transformation strategy from imine-COFs to Am-COFs, we substituted the linkers in PyTTA-BPDA-COF (36) (fig. S6, scheme S2) and TAPB-DMTP-COF (37) (fig. S7, scheme S3) with BDBP and 1,1′-(1,4-phenylene)bis(2-bromoethan-1-one) (PBB), respectively, producing Am-COF-2 (figs. S8A and S9) and Am-COF-3 (Fig. 2A, scheme S3, and figs. S8B and S10) with varied pore sizes and topologies. A model compound, 1-phenyl-2-(phenylamino) ethan-1-one (scheme S4), had its structure confirmed by nuclear magnetic resonance (NMR) spectroscopy and high-resolution mass spectrometry.

Transformations in chemical composition from imine-COFs to Am-COFs (fig. S11) were evidenced by Fourier transform infrared (FT-IR) spectroscopy (fig. S12) and solid-state $^{13}$C cross-polarization magic-angle-spinning NMR spectroscopy ($^{13}$C CP/MAS NMR, fig. S13). The experimental powder x-ray diffraction (PXRD) patterns of the resulting COFs matched the simulated patterns based on eclipsed stacking models (Fig. 2B, fig. S14, and tables S4 to S7),

[1]Key Laboratory of Cluster Science, Ministry of Education, Beijing Key Laboratory of Photoelectronic/Electrophotonic Conversion Materials, Frontiers Science Center for High Energy Material, Advanced Technology Research Institute (Jinan), School of Chemistry and Chemical Engineering, Beijing Institute of Technology, Beijing 100081, P. R. China.
[2]CAS Key Laboratory of Mechanical Behavior and Design of Materials, Department of Modern Mechanics, University of Science and Technology of China, Hefei 230022, P. R. China.
[3]Wuhan Institute of Marine Electric Propulsion, Wuhan Hydrogen Fuel Cell Engineering Research Center, Wuhan 430064, P. R. China.
*Corresponding author. Email: bowang@bit.edu.cn (B.W.); fengxiao86@bit.edu.cn (X.F.)

verifying the structural changes. High-resolution transmission electron microscopy (HRTEM, Fig. 2, E and F, and figs. S15 to S17) and nitrogen sorption isotherms (Fig. 2C and fig. S18) further confirmed the mesoporous structures, with pore size distributions (Fig. 2D and fig. S19) aligning with the structural modifications. Thermogravimetric analyses demonstrated that the decomposition temperatures of all synthesized Am-COFs exceeded 200°C (fig. S20).

The Am-COFs formed as two-dimensional polymeric sheets linked by molecular building units that created periodic polygons and well-organized one-dimensional nanochannels with functionalized pore walls for efficient mass transport. Among the obtained Am-COFs, Am-COF-3 emerged as the most effective ionomer in the initial single-cell experiments, which we attributed to its optimal morphology, pore size, and channel density. To further improve COF dispersion and minimize phase separation with other components in the CL, we modified Am-COF-3 by grafting sodium propanesulfonic acid onto its pore walls (Fig. 2A). Elemental analyses revealed a grafting rate of 12%, which was equivalent to approximately one sulfonic acid per polygon. The ideal and apparent ion exchange capacity of Am-COF-3-$SO_3H$ is 0.36 and 0.30 milliequivalent per gram, respectively.

The resulting Am-COF-3-$SO_3H$ inherited high crystallinity (Fig. 2B) and porosity (Fig. 2C), and the grafting was verified by $^{13}C$ CP/MAS NMR, IR, and x-ray photoelectron spectroscopy (XPS) (fig. S21). Am-COF-3-$SO_3H$ had high colloidal stability in water (fig. S22). Morphological analysis through transmission electron microscopy (TEM) (fig. S23) and atomic force microscopy (AFM) (fig. S24) showed that Am-COF-3-$SO_3H$ formed with as nanosheets with an average thickness of 1.6 to 1.9 nm. Considering the vulnerability of the CL to oxidative damage (38, 39), the chemical stability of Am-COF-3-$SO_3H$ was tested under Fenton's condition. The chemical structure of Am-COF-3-$SO_3H$ showed no obvious change as revealed by IR spectra (fig. S25).
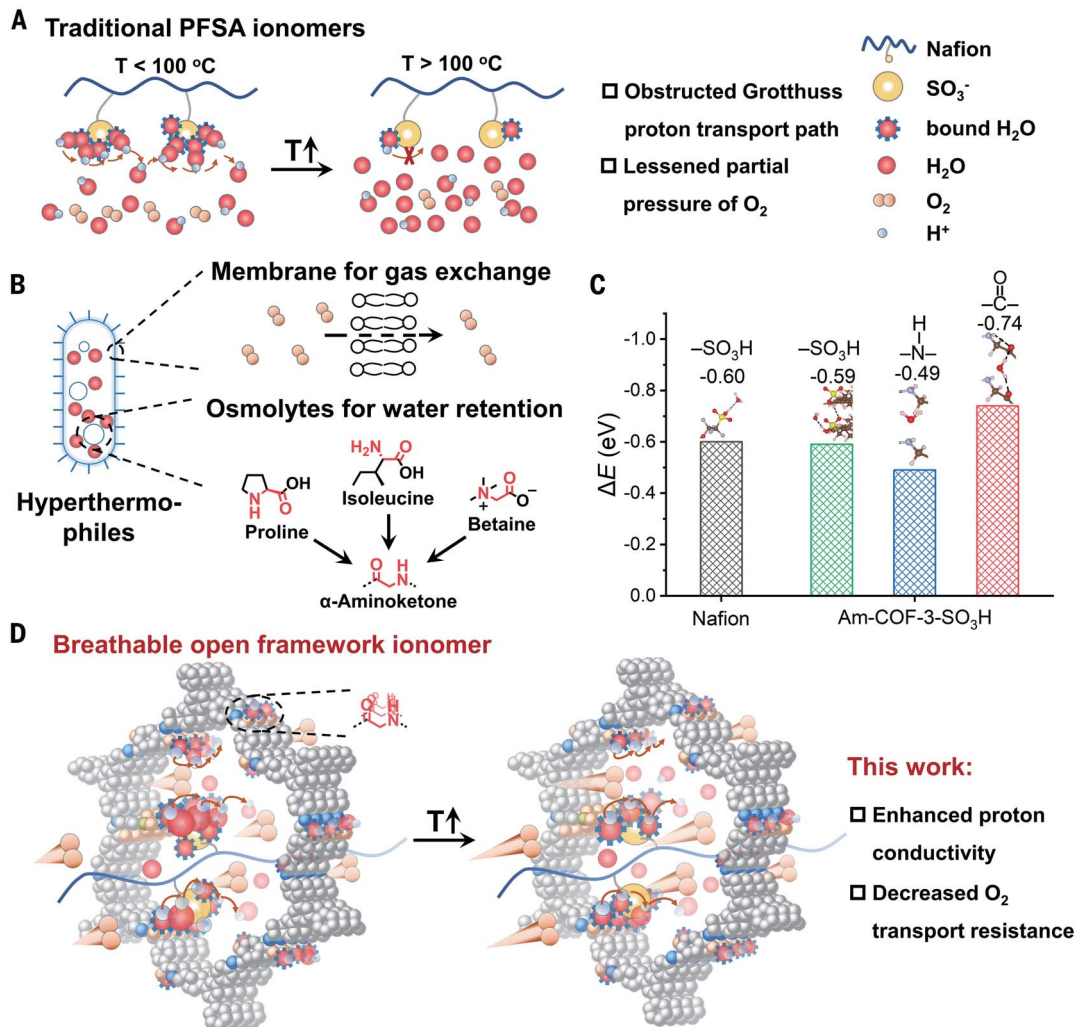
### Water retention of Am-COF-3-$SO_3H$

Water retention abilities, crucial for facilitating proton Grotthuss hopping transport, were initially evaluated with in-situ diffuse reflectance FT-IR spectroscopy (DRIFTS). We recorded DRIFTS spectra (Fig. 3A) for Am-COF-3-$SO_3H$ and Nafion, each adsorbed with a drop of water, at 80°C. Peak deconvolution in the 3800 to 3200 $cm^{-1}$ region revealed that the peaks at 3640, 3604, 3540, and 3464 $cm^{-1}$ corresponded to free water and water bound to N—H, —$SO_3H$, and C=O functional groups, respectively, with the peak at 3361 $cm^{-1}$ identified as the N—H stretching vibration (table S8). Further in situ DRIFTS analysis (Fig. 3B and fig. S26) at 105°C and 80% relative humidity (RH) revealed a stretching vibration peak at 3450 $cm^{-1}$ for water bound to C=O in Am-COF-3-$SO_3H$ (40), whereas Nafion did not exhibit any characteristic bound water molecule peaks, although the primary hydration shells may still be present (41, 42).

Additionally, at 80°C and 100% RH, the water stretching vibration peak in Am-COF-3-$SO_3H$ exhibited a redshift compared with that in Nafion, indicating a stronger interaction with water molecules. This finding was corroborated by the redshift of the C=O stretching vibration in Am-COF-3-$SO_3H$ caused by increasing humidity (Fig. 3B). As evidenced by the water sorption isotherms at 25° and 60°C,



**Fig. 1. Mass transport within ionomers and water adsorption energy.** (**A**) Proton and oxygen transport within a traditional PFSA ionomer in LT and MT PEMFCs. (**B**) Hyperthermophiles enable gas exchange and water retention under extreme conditions. (**C**) Binding energy of a water molecule at different sites within Nafion (—$SO_3H$) and Am-COF-3-$SO_3H$ (—$SO_3H$, N–H, and C=O). (**D**) Proton and oxygen transport within a breathable open framework ionomer in LT and MT PEMFCs.

the water sorption capacity of Am-COF-3-SO$_3$H increased with rising temperature at low partial pressures. We attributed this phenomenon to the increased flexibility of the framework at higher temperature facilitating the formation of multiple hydrogen bonds with guest water molecules (Fig. 3C and fig. S27). Furthermore, the hysteresis loops observed in the water sorption isotherms of Am-COF-3-SO$_3$H (Fig. 3D) that were absent in Nafion suggested that adsorbed water molecules were more difficult to remove from Am-COF-3-SO$_3$H (43).

## Proton transportation in MEA

In LT (80°C, 100% RH) and MT (105°C, 80% RH) PEMFC single-cell tests, we used a blend of Am-COF-3-SO$_3$H/Nafion (mass ratio = 1:3) along with commercial Pt/C (Pt/Vulcan, cathode loading: 0.1 mg$_{Pt}$ cm$^{-2}$) as ionomer and catalyst, respectively. We maintained a fixed ionomer to carbon (I/C) ratio of 0.8 (44, 45) using Nafion N212 as the proton exchange membrane (PEM) in the MEA. TEM (fig. S28) and energy dispersive x-ray spectroscopy (figs. S29 to S31), along with AFM (46) (figs. S32 to S34), showed that a uniform coating of Am-COF-3-SO$_3$H and Nafion formed on the surface of the Pt/C catalyst in the CL. Under H$_2$-O$_2$ feed conditions (150 kPa back pressure), the Pt/C@Am-COF-3-SO$_3$H/Nafion fuel cell achieved peak power densities of 2.17 W cm$^{-2}$ at 80°C (100% RH, fig. S35) and 1.87 W cm$^{-2}$ at 105°C (80% RH, Fig. 4A). These values represent enhancements of 1.21 and 1.33 times, respectively, compared with control MEA without Am-COF-3-SO$_3$H. The H$_2$-air tests revealed a similar improvement in MEA power performance upon the introduction of COF (fig. S36). After accelerated stress tests (AST) at 105°C for 30,000 cycles, the rated current density (@0.67 V) of the Am-COF-3-SO$_3$H/Nafion-based MEA maintained 54% of its initial value, compared with 44% for the Nafion-based MEA (figs. S37 and S38). XPS analyses (fig. S39) revealed that the COF skeleton remained stable whereas degradation in Nafion was observed, contributing to the performance decline after AST.

Electrochemical impedance spectroscopy (EIS) was conducted to investigate proton conduction (fig. S40). Through an analysis of the distribution of relaxation times (DRT) (47, 48) (Fig. 4B), we determined the mass transport resistance within the MEA during H$_2$-O$_2$ tests, particularly focusing on the ohmic polarization region, where proton transport resistance dominated. The increase in proton transport resistance after raising the operating temperature from 80° to 105°C was lower for Pt/C@Am-COF-3-SO$_3$H/Nafion than for Pt/C@Nafion.

We conducted EIS measurements under H$_2$-N$_2$ conditions at 0.5 V to further isolate and assess the proton conduction resistance ($R_{H^+}$) within the CL, distinguishing it from the overall $R_{H^+}$ observed in the MEA (49, 50). For the Pt/C@Am-COF-3-SO$_3$H/Nafion-based CL, $R_{H^+}$ decreased from 0.187 to 0.164 ohm as the temperature was raised from 80° to 105°C, contrasting with Pt/C@Nafion, where it increased from 0.190 to 0.322 ohm (Fig. 4C and fig. S41). This observation suggests that the rise in proton transport resistance within the Pt/C@Am-COF-3-SO$_3$H/Nafion-based MEA at elevated temperature is primarily attributed to the PEM (Nafion N212).

We assessed $R_{H^+}$ in Pt/C@Nafion and Pt/C@Am-COF-3-SO$_3$H/Nafion-based CL across a range of temperatures under 80% RH (fig. S42). The proton conductivities were determined by considering the thickness of the catalyst layer (figs. S43 and S44) as the equivalent proton transport in the H$_2$-N$_2$ tests (51, 52). Arrhenius plots were fit to determine the activation energies for proton transport within the CLs (Fig. 4D), a measure not influenced by the presumed path length for proton transport. For the Pt/C@Nafion-based CL, an activation energy of 0.43 eV was recorded for temperatures below 100°C, suggesting a mixed Grotthuss and vehicle mechanism for proton transport (53, 54). However, a notable decrease in proton conductivity was observed as temperatures exceeded 100°C, signaling a disruption in the
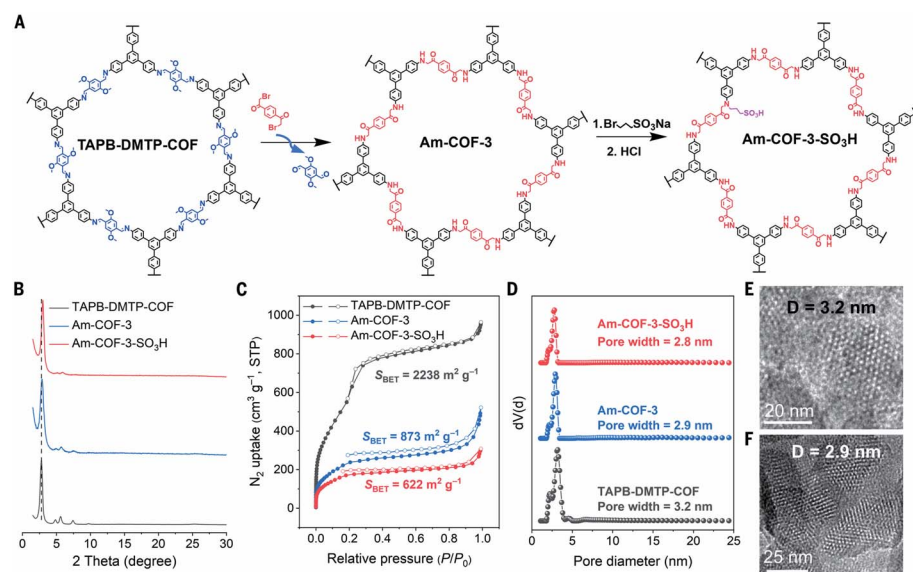


**Fig. 2. Synthesis and characterization of breathable open framework ionomer.** (**A**) Synthetic route of Am-COF-3-SO$_3$H. (**B**) PXRD patterns, (**C**) N$_2$ sorption isotherms, and (**D**) pore size distribution of TAPB-DMTP, Am-COF-3, and Am-COF-3-SO$_3$H. (**E**) and (**F**) HRTEM images of (E) TAPB-DMTP-COF and (F) Am-COF-3.
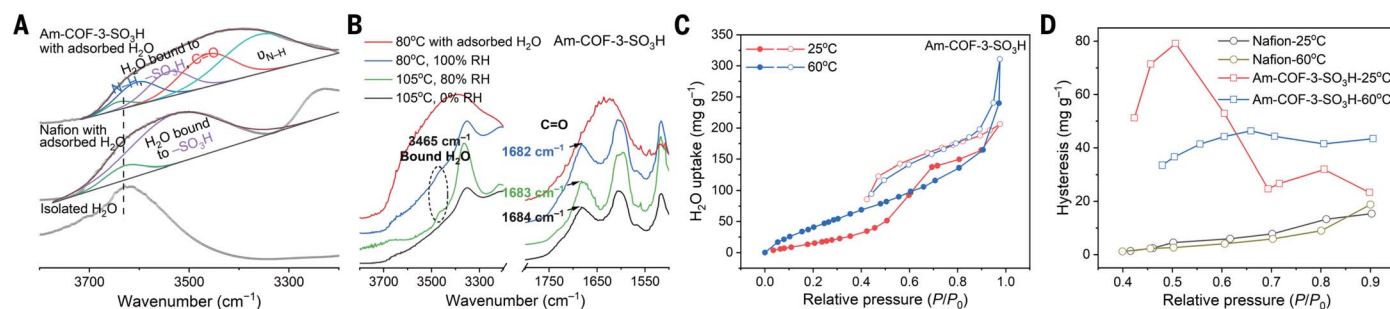


**Fig. 3. Water retention.** (**A**) DRIFTS spectra for Am-COF-3-SO$_3$H and Nafion: Peak deconvolution in the 3800 to 3200 cm$^{-1}$ of ionomers adsorbed with a drop of water and isolated water at 80°C and (**B**) spectra of Am-COF-3-SO$_3$H under different conditions. (**C**) H$_2$O sorption isotherms of Am-COF-3-SO$_3$H at 25° and 60°C. (**D**) H$_2$O hysteresis plots of Nafion and Am-COF-3-SO$_3$H at 25° and 60°C.
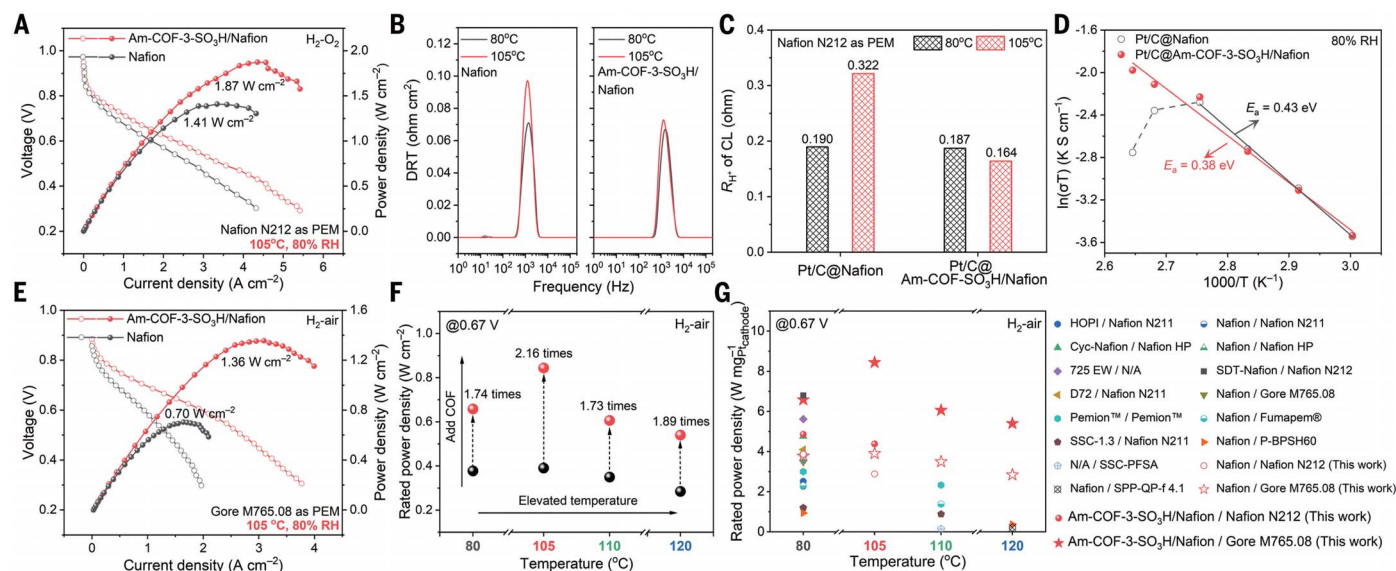
**Fig. 4. Proton transport and fuel cell performance.** (**A**) $H_2$-$O_2$ fuel cell *I-V* polarization and power density plots with Pt/C@Nafion and Pt/C@Am-COF-3-SO$_3$H/Nafion (1:3) measured at 105°C and 80% RH under 150 kPa$_{BP}$ (Nafion N212 as PEM). (**B**) DRT plots of Nafion and Am-COF-3-SO$_3$H/Nafion-based MEAs in $H_2$-$O_2$ test at 80°C (100% RH) and 105°C (80% RH), in which the peak represents the proton transport resistance. (**C**) $R_{H^+}$ within the CL and (**D**) Arrhenius plots of Pt/C@Nafion and Pt/C@Am-COF-3-SO$_3$H/Nafion. (**E**) $H_2$-air fuel cell *I-V* polarization and power density plots with Pt/C@Nafion

and Pt/C@Am-COF-3-SO$_3$H/Nafion (1:3) measured at 105°C and 80% RH under 200 kPa$_{BP}$ (Gore M765.08 as PEM, cathode loading: 0.1 mg$_{Pt}$ cm$^{-2}$, anode loading: 0.1 mg$_{Pt}$ cm$^{-2}$). (**F**) Comparison of the rated power densities of MEAs evaluated under $H_2$-air conditions at 80°C (100% RH), 105°C (80% RH), and 110°C (70% RH) (Cathode loading: 0.1 mg$_{Pt}$ cm$^{-2}$, anode loading: 0.1 mg$_{Pt}$ cm$^{-2}$). (**G**) Comparing the rated power density per Pt loading for MEAs based on commercial Pt/C catalyst in this study and other reported works (table S9).

proton conduction pathway. Conversely, the Pt/C@Am-COF-3-SO$_3$H/Nafion-based CL showed an activation energy of 0.38 eV over a broader temperature range, from 60° to 105°C. This result indicates that the incorporation of Am-COF-3-SO$_3$H into the CL enabled proton conduction primarily through the Grotthuss mechanism, which remained unaffected by changes in temperature even beyond the 100°C threshold.

## Fuel cell performance

To mitigate the impact of PEM on the proton conduction at medium operating temperatures, we replaced Nafion N212 (50 μm thickness) in MEA with Gore M765.08 (8 μm) and optimized the CL composition (figs. S45 to S47). In $H_2$-air tests (200 kPa$_{BP}$), the peak power density for the MEA incorporating the COF reached 1.36 W cm$^{-2}$ with good repeatability (Fig. 4E and fig. S48). Its rated power density (@0.67 V) at 80°, 105°, 110°, and 120°C was 1.74, 2.16, 1.73, and 1.89 times higher (Fig. 4F and fig. S49), respectively, compared with the control MEA without the COF. The Pt loading was further reduced to 0.07 mg cm$^{-2}$ (figs. S50 and S51) and the achieved peak and rated power density per Pt loading (18.1 and 9.5 W mg$^{-1}_{Pt cathod}$ at 105°C; 14.6 and 7.5 mg$^{-1}_{Pt cathod}$ at 110°C) exceeded those of previously reported cell performance using commercial Pt/C as the catalyst (Fig. 4G and table S9). No apparent performance deterioration was observed with reduced gas flow rate (figs. S52).

Additionally, we synthesized amorphous Am-COF-3-SO$_3$H (a-Am-COF-SO$_3$H) (fig. S53) and a crystalline sample with a higher —SO$_3$H grafting rate up to 28% (Am-COF-3-SO$_3$H-h) (fig. S54). Fuel cell performance tests at 105°C revealed that although the Am-COF-3/Nafion-, a-Am-COF- SO$_3$H/Nafion- and Am-COF-3-SO$_3$H-h/Nafion-based MEAs outperformed pure Nafion (figs. S55 to S57), the enhancements were less pronounced compared with the Am-COF-3-SO$_3$H/Nafion-based MEA. Furthermore, we used polystyrene sulfonic acid (PSA) instead of Nafion in the catalyst layer. The peak power density of the MEA based on Am-COF-3-SO$_3$H/PSA at 105°C was 1.24 and 1.50 times higher than those with pure Nafion or pure PSA, respectively (Fig. 4E and fig. S58).

Open-circuit voltage (OCV) tests conducted at 90°C and 30% RH revealed that after 120 hours, the voltage retention remained at 80% of its initial value (fig. S59), with hydrogen crossover current density below 15 mA cm$^{-2}$ (fig. S60). The CO tolerance was assessed with a 50 parts per million (ppm) CO and $H_2$ mixture (9). At 105°C, the reduction in peak power density was less compared with the reduction at 80°C (figs. S61 to S63), proving enhanced CO tolerance at higher operating temperatures.

## Mechanism discussions

EIS and DRT analyses (fig. S64) revealed that proton transport resistances of Pt/C@Am-COF-

3-SO$_3$H/Nafion-based MEA (Gore M765.08 as PEM) were lower than those of Pt/C@Nafion-based MEA. The deduced $R_{H^+}$ in the CL at elevated temperatures (figs. S65 and S66) was also reduced after incorporating COF.

$O_2$ mass transport resistance within the cell was determined from the limiting current density measurements, with the total $O_2$ transport resistance ($R_{tot}$, fig. S67) comprising both pressure-dependent resistance ($R_P$) and pressure-independent resistance ($R_{NP}$) (45, 55). $R_P$ is associated with gas diffusion in the flow field channels and through the larger voids among agglomerates in the CL, whereas $R_{NP}$ primarily stems from Knudsen diffusion in smaller mesopores and the resistance for $O_2$ penetration from the ionomer thin films to the active sites. The calculated $R_{NP}$ for Am-COF-3-SO$_3$H/Nafion (7.6 s m$^{-1}$ at 105°C, 21.6 s m$^{-1}$ at 80°C) was lower than that for Nafion alone (45.9 s m$^{-1}$ at 105°C, 81.8 s m$^{-1}$ at 80°C) (Fig. 5, A and B). Theoretically, $R_P$ would be expected to decrease inversely with temperature to the power of −1.75 within a certain range (56). This theoretical prediction was verified by the performance of the Am-COF-3-SO$_3$H/Nafion-based single fuel cell, where $R_P$ was reduced from 80° to 105°C (Fig. 5C and fig. S68). However, in the Nafion-based single fuel cell, the experimental reduction in $R_P$ was less pronounced than expected, likely because of increased water vapor pressure and the consequent decrease in $O_2$ partial pressure resulting from

Nafion dehydration at the 105°C. These findings not only demonstrated a notable reduction in $O_2$ mass transport resistance, but also affirmed the improved water retention capabilities provided by integrating Am-COF-3-SO$_3$H. In addition, we prepared condensed Am-COF-3-SO$_3$H/Nafion and Nafion composite membranes (fig. S69) for gas permeability measurements; the results (fig. S70) also confirmed the role of the open framework in reducing oxygen transport resistance.

Ultrahigh-speed variable-temperature $^1$H ssNMR analyses confirmed entrapment of Nafion chains within Am-COF-3-SO$_3$H pores. Notably, in the spectrum of Am-COF-3-SO$_3$H/Nafion obtained from the ink (Fig. 5D), compared with those of Nafion alone and a simple mixture with Am-COF-3-SO$_3$H (denoted as Am-COF-3-SO$_3$H *mix.* Nafion), the downfield shift of −SO$_3$H from 9.20 to 9.78 parts per million (ppm) and the upfield shift of N−H protons from 4.90 to 4.52 ppm indicated intermolecular hydrogen bonding between Am-COF-3-SO$_3$H's polar pore walls and Nafion's sulfonic acid groups. Variable-temperature experiments further demonstrated the temperature-dependent dynamics of these hydrogen bonds, with −SO$_3$H peaks shifting upfield from 9.78 to 9.61 ppm as temperature increased, indicating a partial disruption of hydrogen bonds (Fig. 5D and fig. S71). Additionally, $^{19}$F ssNMR analyses revealed minimal differences between Am-COF-3-SO$_3$H

*mix.* Nafion and Am-COF-3-SO$_3$H/Nafion, suggesting negligible interaction of −C−F groups with the pore walls (fig. S72).

Dynamic vapor sorption measurements indicated a higher water content around per SO$_3^-$ of Nafion in Am-COF-3-SO$_3$H/Nafion than Nafion alone in different relative humidity at 298 K (Fig. 5E and table S10). Simultaneously, the water sorption isotherms of Am-COF-3-SO$_3$H/Nafion exhibited an increased water adsorption capacity with rising temperature, similar to the case of Am-COF-3-SO$_3$H (fig. S73). The H$_2$O temperature programmed desorption (TPD) analysis revealed that a higher desorption peak temperature for H$_2$O in Am-COF-3-SO$_3$H/Nafion compared with Nafion alone (Fig. 5F), demonstrating a stronger affinity of Am-COF-3-SO$_3$H/Nafion for H$_2$O. We built simplified models of Am-COF-3-SO$_3$H/Nafion and Nafion, each incorporating four water molecules, and performed DFT calculations (figs. S74 to S76, table S11). For the Am-COF-3-SO$_3$H/Nafion composite, the computed binding energy ($\Delta E$) was −3.67 eV. At 105°C, the enthalpy change ($\Delta H$) was −3.34 eV, and the free energy change ($\Delta G$) value was −0.81 eV. These values are more negative compared with that of the Nafion model, which had $\Delta E$, $\Delta H$, and $\Delta G$ values of −2.76, −2.47, and −0.04 eV, respectively. A polygon structure model of Am-COF-3-SO$_3$H/Nafion was then constructed for molecular

dynamics (MD) simulations. The results (fig. S77) demonstrated that proton conduction predominantly occurred along water chains aligned between Am-COF-3-SO$_3$H and Nafion structures through a Grotthuss mechanism. The experimental and theoretical calculation results demonstrated that Nafion segments penetrated the COF channels, synergistically stabilizing water molecules through multiple hydrogen bonds, thereby preserving proton transport pathways under MT working conditions.

## Conclusions

The incorporation of "breathable" open framework ionomers into the CL of medium-temperature PEMFCs created a microenvironment that not only improved water retention but also ensures gas permeability. α-Aminoketone–linked Am-COF-3-SO$_3$H stabilized water molecules through synergistic hydrogen bonding, allowing Grotthuss proton hopping for efficient conduction and accelerating oxygen mass transport within the fuel cells. Furthermore, this approach mitigated Pt poisoning (fig. S78), a common challenge posed by the sulfonic acid groups of Nafion (57, 58). This breakthrough underscores the potential of crystalline ionomers to address fundamental challenges in MT PEMFCs for enhancing fuel cell performance at both low and medium operating temperatures. Such versatility is critical for practical applications,
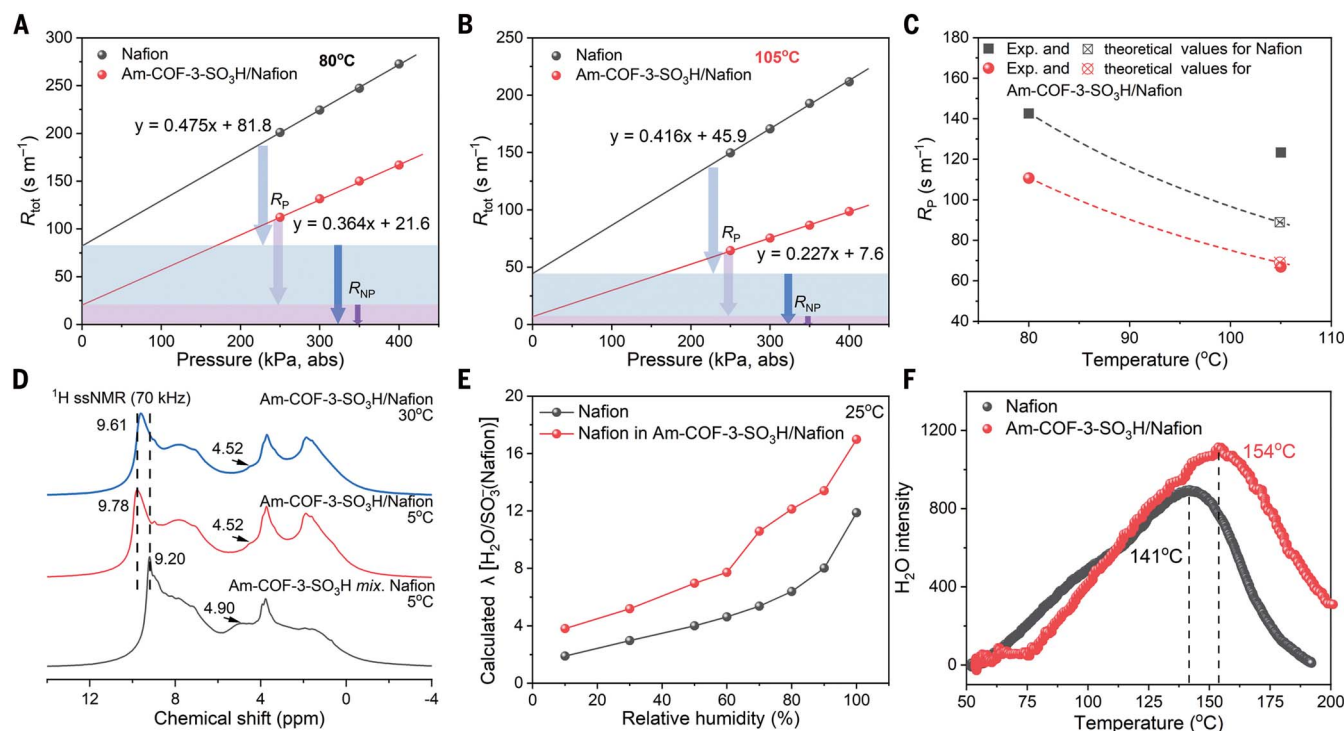
**Fig. 5. Oxygen transport and host-guest interaction.** (**A**) and (**B**) Variation in $R_{tot}$ for Nafion and Am-COF-3-SO$_3$H/Nafion–based FC as a function of absolute pressure at (A) 80°C and (B) 105°C. (**C**) Experimental and theoretical deduced $R_P$ for Nafion and Am-COF-3-SO$_3$H/Nafion–based FC under 300 kPa abs. (**D**) Ultrahigh-speed variable-temperature $^1$H ssNMR of Am-COF-3-SO$_3$H/Nafion and Am-COF-3-SO$_3$H *mix.* Nafion. (**E**) Calculated water content around per SO$_3^-$ in Nafion (λ [H$_2$O/SO$_3^-$ (Nafion)]) for pure Nafion and Nafion in Am-COF-3-SO$_3$H/Nafion in different relative humidity at 25°C. (**F**) H$_2$O TPD tests for Nafion and Am-COF-3-SO$_3$H/Nafion.

in which low temperatures are preferred for steady-state operations and medium temperatures are beneficial for high-power demands over short durations.

## REFERENCES AND NOTES

1. K. Jiao et al., Nature **595**, 361–369 (2021).
2. X. Tian, X. F. Lu, B. Y. Xia, X. W. Lou, Joule **4**, 45–68 (2020).
3. D. A. Cullen et al., Nat. Energy **6**, 462–474 (2021).
4. C. Lee et al., Nat. Energy **8**, 685–694 (2023).
5. Z. Zhao et al., Nat. Nanotechnol. **17**, 968–975 (2022).
6. Y. S. Kim, Adv. Sci. **10**, e2303914 (2023).
7. R. Haider et al., Chem. Soc. Rev. **50**, 1138–1187 (2021).
8. Q. Meyer, C. Yang, Y. Cheng, C. Zhao, Electrochem. Energy Rev. **6**, 16 (2023).
9. Q. Li, R. He, J.-A. Gao, J. O. Jensen, N. J. Bjerrum, J. Electrochem. Soc. **150**, A1599–A1605 (2003).
10. J. Zhang et al., J. Power Sources **160**, 872–891 (2006).
11. A. Kongkanand, M. F. Mathias, J. Phys. Chem. Lett. **7**, 1127–1137 (2016).
12. K. H. Lim et al., Nat. Energy **7**, 248–259 (2022).
13. D. Aili et al., J. Electrochem. Soc. **167**, 134507 (2020).
14. X. Li et al., Chem. Mater. **32**, 1182–1191 (2020).
15. H. Tang et al., Nat. Energy **7**, 153–162 (2022).
16. H. Tang et al., Nat. Commun. **13**, 7577 (2022).
17. NEDO, "Japanese New Energy and Industrial Technology Development Organization (NEDO) FCV·HDV fuel cell technology development roadmap" (2023); https://www.nedo.go.jp/content/100956710.pdf.
18. C. H. Park et al., Nature **532**, 480–483 (2016).
19. P. Guan et al., Sci. Adv. **9**, eadh1386 (2023).
20. Z. Long, K. Miyatake, ACS Appl. Mater. Interfaces **13**, 15366–15372 (2021).
21. H. Nguyen et al., Sustain. Energy Fuels **5**, 3687–3699 (2021).
22. J. Zhang et al., Electrochim. Acta **53**, 5315–5321 (2008).
23. J. Zhang, Y. Tang, C. Song, J. Zhang, H. Wang, J. Power Sources **163**, 532–537 (2006).
24. A. P. Côté et al., Science **310**, 1166–1170 (2005).
25. X. Feng, X. Ding, D. Jiang, Chem. Soc. Rev. **41**, 6010–6022 (2012).
26. X. Huang, C. Sun, X. Feng, Sci. China Chem. **63**, 1367–1390 (2020).
27. X. Wu et al., J. Am. Chem. Soc. **142**, 14357–14364 (2020).
28. A. Ozden et al., Nat. Energy **8**, 179–190 (2023).
29. Q. Zhang et al., Science **378**, 181–186 (2022).
30. C. Vieille, G. J. Zeikus, Microbiol. Mol. Biol. Rev. **65**, 1–43 (2001).
31. K. O. Stetter, Philos. Trans. R. Soc. B **361**, 1837–1842 (2006).
32. P. H. Yancey, M. E. Clark, S. C. Hand, R. D. Bowlus, G. N. Somero, Science **217**, 1214–1222 (1982).
33. C. Qian et al., J. Am. Chem. Soc. **139**, 6736–6743 (2017).
34. Z. B. Zhou et al., Nat. Commun. **13**, 2180 (2022).
35. M. Matsumoto et al., J. Am. Chem. Soc. **139**, 4999–5002 (2017).
36. F. Auras et al., J. Am. Chem. Soc. **138**, 16703–16710 (2016).
37. P. Wang et al., Adv. Mater. **30**, e1801991 (2018).
38. C. Y. Ahn et al., Chem. Rev. **121**, 15075–15140 (2021).
39. S. Mo et al., Electrochem. Energy Rev. **6**, 28 (2023).
40. G. E. M. Schukraft et al., J. Phys. Chem. B **126**, 8048–8057 (2022).
41. A. Kusoglu, A. Z. Weber, Chem. Rev. **117**, 987–1104 (2017).
42. L. Wadsö, P. Jannasch, J. Phys. Chem. B **117**, 8561–8570 (2013).
43. C.-M. Popescu, C. A. S. Hill, R. Anthony, G. Ormondroyd, S. Curling, Polym. Degrad. Stabil. **111**, 263–268 (2015).
44. A. Suzuki et al., Int. J. Hydrogen Energy **36**, 2221–2229 (2011).
45. Y. V. Yakovlev et al., J. Power Sources **490**, 229531 (2021).
46. T. Morawietz, M. Handl, C. Oldani, K. A. Friedrich, R. Hiesgen, ACS Appl. Mater. Interfaces **8**, 27044–27054 (2016).
47. T. H. Wan, M. Saccoccio, C. Chen, F. Ciucci, Electrochim. Acta **184**, 483–499 (2015).
48. Z. Tang et al., J. Power Sources **468**, 228361 (2020).
49. D. Malevich et al., J. Electrochem. Soc. **159**, F888–F895 (2012).
50. H. Ren et al., J. Power Sources **506**, 230186 (2021).
51. G. Wang, L. Osmieri, A. G. Star, J. Pfeilsticker, K. C. Neyerlin, J. Electrochem. Soc. **167**, 044519 (2020).
52. A. Kulikovsky, Electrochem. Sci. Adv. **1**, e2000023 (2020).
53. G. Xu, K. Otsubo, T. Yamada, S. Sakaida, H. Kitagawa, J. Am. Chem. Soc. **135**, 7438–7441 (2013).
54. Y. Ye et al., J. Am. Chem. Soc. **139**, 15604–15607 (2017).
55. R. Jinnouchi et al., Nat. Commun. **12**, 4956 (2021).
56. N. Nonoyama, S. Okazaki, A. Z. Weber, Y. Ikogi, T. Yoshida, J. Electrochem. Soc. **158**, B416–B422 (2011).
57. K. Kodama et al., ACS Catal. **8**, 694–700 (2017).
58. F. Chen et al., Nat. Catal. **6**, 392–401 (2023).

## SUPPLEMENTARY MATERIALS

science.org/doi/10.1126/science.adq2259
Materials and Methods
Figs. S1 to S78
Tables S1 to S11
References (59–78)

Submitted 3 May 2024; accepted 1 August 2024
10.1126/science.adq2259